university of groningen

faculty of science and engineering

Timing Performance of Plastic Scintillator Detectors for n_TOF Applications

Author:
Rutger WIJNSEMA
(s4957563)

Supervisor:
prof. M. KAVATSYUK
Second examiner :
prof. George PALASANTZAS

Bachelor's Thesis
To fulfill the requirements for the degree of
Bachelor of Science in Applied Physics
at the University of Groningen

November 23, 2025

Contents

Page

Abstract **4**

1 Introduction **5**

2 Background Literature **6**
2.1 Plastic Scintillator Detectors 6
2.1.1 Plastic Scintillators 6
2.1.2 Photomultiplier Tubes 6
2.1.3 Digitizers 7
2.2 Cosmic Muons 7
2.3 Constant Fraction Discrimination 7
2.4 Energy Estimation Using Geometric Mean 8
2.5 Determination of Energy Resolution 9
2.5.1 Time Resolution 9
2.5.2 Effective light velocity in the scintillator 9
2.5.3 Spatial Resolution 10
2.5.4 Energy Determination 10

3 Experimental Methods **11**
3.1 Experimental Setup 11
3.2 Software Configuration 11
3.3 Measurement Procedure 12

4 Results **13**
4.1 Overview of Data Processing 13
4.2 Baseline Correction 13
4.3 Gain Matching 14
4.4 CFD Optimization 15
4.5 Determination of Effective Velocity 16
4.6 Determination of Resolutions 17

5 Discussion **18**
5.1 Accuracy of Experiment 18
5.1.1 Gain Matching 18
5.1.2 CFD 18
5.1.3 Effective Velocity 18
5.2 Importance of Timing Accuracy 19
5.3 Application at n_TOF 19

6 Conclusion **21**

Bibliography **22**

Appendices **24**
A Analysis Code 24
B Error Propagation 24
B.1 Effective Velocity 24
B.2 Spatial Resolution 24

Abstract

This thesis investigates the timing performance of plastic scintillator detectors for use in the proton recoil telescope (PRT) at CERN's n_TOF facility. Since the ESRIG laboratory has no neutron beam available, downward cosmic muons were used as substitute to study detector properties. Measurements were performed with several detector separations (0-30 cm) to study how geometry affects timing resolution, spatial resolution and coincidence rates. Each dataset with 5000 acquisitions was analyzed using baseline correction, gain matching and a constant fraction discriminator (CFD).

The plastic scintillator detectors showed excellent timing performance. A per-bar time resolution of 0.18 ns and a spatial resolution of $\sim 3.1 \pm 0.4$ cm were achieved. Larger separation select more perpendicular muon trajectories, however, also reduce coincidence rate significantly. A separation of 20 cm provided the best balance between these factors.

Applying these results to the n_TOF PRT, where recoil protons travel 5 meters between start and stop detectors, the timing precision corresponds to a fractional energy uncertainty at the percent level. This demonstrates that plastic scintillator detectors provide sufficient timing performance for proton time-of-flight measurements and are therefore suitable for n_TOF application.

1 Introduction

The neutron-induced fission cross section of ^{235}U is one of the most important standard reference quantities in nuclear physics. It is used for many applications ranging from neutron detector calibration to fundamental studies of neutron-nucleus interactions. Above 200 MeV, there is not much data which motivates new measurements in this region [1]. The n_TOF (neutron time-of-flight) facility at CERN provides a neutron beam with a wide energy spectrum. This neutron beam is produced by directing a high-energy proton beam onto a lead target, where spallation reactions in the lead nuclei emit large numbers of neutrons. The neutrons then travel a long flight of 185 meters to the experimental area [1].

In the experimental area there are several detector systems monitoring flux and reaction rates. One of these is the proton recoil telescope, which measures the neutron energy by detecting recoil protons after elastic scattering in polyethylene [2]. In this experiment, plastic scintillator detectors are investigated to assess whether they are suitable for measuring the recoil protons. These protons are detected in a start detector and then again in a stop detector located about 5 meters further away [2].

In time-of-flight measurements, the timing performance of the detector is important. The energy resolution follows the relation $\Delta E/E = 2\Delta T/T$ [3]. Therefore, for a fixed flight path, a low time resolution improves $\Delta E/E$.

This thesis describes an experiment investigating the timing performance of plastic scintillator detectors for multiple detector separations. As the ESRIG facility at the Rijksuniversiteit Groningen does not have a neutron beam, cosmic muons are used to investigate how this separation influences the timing and spatial resolution of these detectors. The purpose was to find the optimal conditions to deduce these detector properties. The separation between the two vertically oriented plastic scintillators is increased as this gives more perpendicular trajectories of the cosmic muons. This means a better-defined interaction position and a situation that resembles the conditions at n_TOF more closely.

2 Background Literature

2.1 Plastic Scintillator Detectors

Plastic scintillator detectors are widely used in time-of-flight measurements. They work as follows: the particle hits the scintillator which emits a certain amount photons equal to the incoming particle's energy. These photons are detected by the photomultiplier tube that converts the photons to an electric signal which can be analyzed through a digitizer.

2.1.1 Plastic Scintillators

When ionizing radiation interacts with matter, it excites many molecules. As these molecules return to their ground state, they can release a photon in or near the visible energy range. This process is called scintillation and is one of the main methods for radiation detection. Not every material can produce a photon with enough energy for detection. Some materials, organic and inorganic, are more efficient and are called scintillators. Plastic scintillators are organic and the most widely used in the industry. Plastic scintillators are based on polymers and can therefore be easily formed in all kinds of shapes. Due to short decay times, the detectors can get precise timing information, which is necessary for time-of-flight applications [4].

2.1.2 Photomultiplier Tubes

A photomultiplier tube (PMT) is a highly sensitive detector that converts weak light signals (even down to single photons) into measurable electric signals. The production of an electric signal follows the following processes. First the photon passes through the input window. The electrons in the photocathode are excited by the energy of the photon and these photoelectrons are emitted into the vacuum. This process is called the external photoelectric effect. The focusing electrode accelerates the photoelectrons onto the first dynode. On these dynodes, the photoelectrons are multiplied by secondary electron emission. These electrons are then collected by the anode, producing an electric signal that is sent to the digitizer [5].

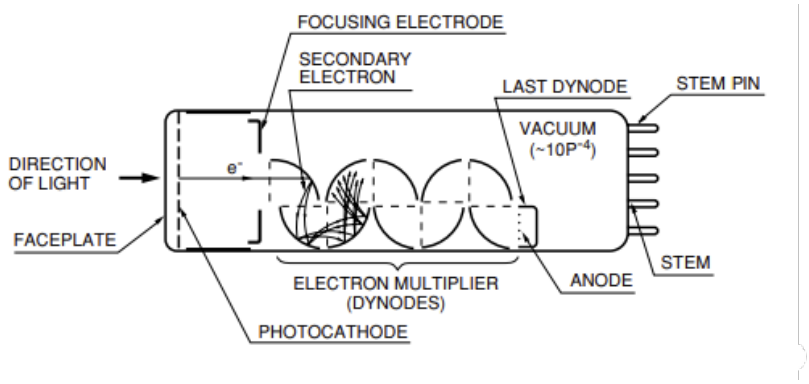

Figure 1: Schematic of a photomultiplier tube.

2.1.3 Digitizers

Digitizers are high-speed devices that convert analog pulses from PMTs into digital waveforms for analysis. In this setup, with plastic scintillator and PMTs, the digitizer replaces analog timing by recording the full pulse shape at high sampling rates. This enables us to extract precise data to investigate pulse's properties like the area and shape. As the whole waveform is available, corrections for time-walk can be applied after acquisition [6, 7]

2.2 Cosmic Muons

The charged particles hitting the scintillator in this experiment are cosmic muons. Cosmic muons are produced high in the atmosphere when primary cosmic rays collide with nuclei, creating pions and kaons. These mesons decay via $\pi^{\pm} \rightarrow \mu^{\pm}\nu_{\mu}$ and $K^{\pm} \rightarrow \mu^{\pm}\nu_{\mu}$ into muons [8]. These muons have a lifetime of only 2.2 μs, however due to their relativistic speeds, they reach the surface of the earth at a few GeV. At the surface, the vertical flux is about 1 muon cm^{-2}min^{-1}, with a wide energy spectrum [9]. The angular distribution is zenith-dependent which scales at a few GeV approximately as [9]:

$$I(\theta) \propto cos^{n}(\theta) \text{ with } n \approx 2 \text{ at sea-level for a few GeV muons} \quad (1)$$

Consequently, more horizontal muons are rarer than vertical muons, and the particle flux drops quickly as the zenith angle increases [10]. The Bethe-Bloch formula states that the mean energy loss per unit path length of a relativistic muon in matter is approximately constant and even decreases a little with higher energies [9].

Detector geometry influences the output signal. When separation between detectors is increased, only muons traveling a more horizontal trajectory trigger both detectors. These more perpendicular tracks have a shorter path inside the scintillator. The deposited energy is proportional to the length of the paths inside the scintillator. Therefore these shorter paths result in smaller pulse amplitudes, even though the underlying dE/dx is constant.

2.3 Constant Fraction Discrimination

Constant Fraction Discrimination (CFD) addresses the challenge of time walk in plastic scintillator detectors. Simple threshold discrimination produces earlier trigger times for larger amplitude pulses, which results in unreliable time-of-flight measurements [11]. CFD solves this limitation by triggering at a constant fraction of the pulse height rather than at a fixed threshold. This decouples the timing from amplitude variations. When the pulse reaches a predetermined fraction of the maximum amplitude, a timing signal is generated [12]. This technique reduces time walk and because of this, timing resolutions of 100 ps can be reached [11]. For neutron flux monitoring, CFD enables precise path reconstruction by providing consistent timing measurements. The zero-point is the point where the pulse goes through zero after implementing the CFD. This zero-point can be utilized to investigate the time and spatial resolution.

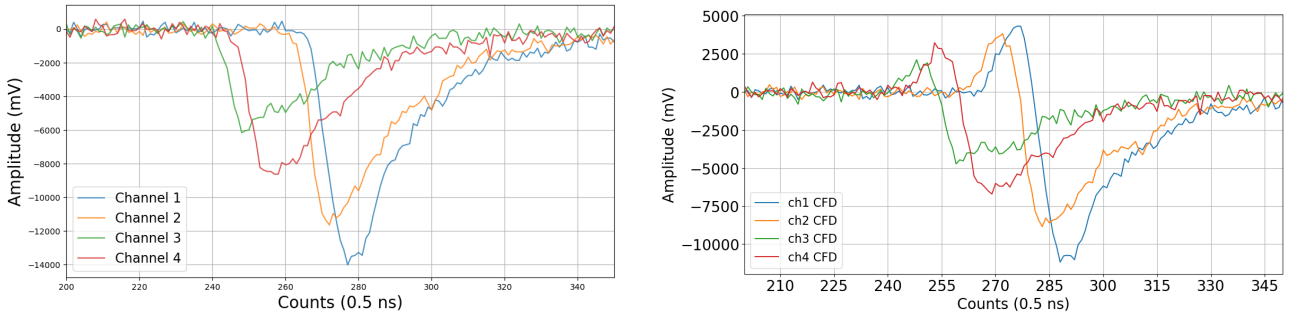

(a) Original pulses

(b) Pulses after CFD

Figure 2: Results of Constant Fraction Discrimination.

The output signal is obtained by forming a bipolar signal from the input pulse. An attenuated copy of the original pulse is subtracted from a delayed version of the same pulse.

$$V_{\text{CFD}}(t) = V_{\text{in}}(t - T_d) - f\,V_{\text{in}}(t) \tag{2}$$

Where f is the fraction that sets the relative amplitude at which the timing signal is taken. The delay T_d aligns the attenuated and delayed pulse to create a precise zero-crossing. Too low fraction increases noise, while too high makes the timing dependent on the pulse shape. A mismatched delay gives an incorrect zero-crossing [13, 14].

2.4 Energy Estimation Using Geometric Mean

Each scintillator bar is read out by two PMTs. When a muon deposits an energy E_0 in the bar, scintillation light is produced and attenuates as it travels to the ends. If the hit is at position x from PMT 1, the integrated pulse area is

$$E_1 \propto G_1\,E_0\,e^{-x/\lambda},\; E_2 \propto G_2\,E_0\,e^{-(L-x)/\lambda} \tag{3}$$

Where G_1 and G_2 are the gains of the PMTs and λ is the attenuation length. To reduce the position dependence, the deposited energy per bar is found using the geometric mean.

$$E_{\text{bar}} = \sqrt{E_1 E_2} \tag{4}$$

From the expressions in Equation 3,

$$E_1 E_2 \propto G_1 G_2\,E_0^2\,e^{-L/\lambda} \tag{5}$$

It is shown that the hit position dependence cancels out. So the energy per bar is then proportional to

$$E_{\text{bar}} \propto E_0\,\sqrt{G_1 G_2}\,e^{-L/(2\lambda)} \tag{6}$$

2.5 Determination of Energy Resolution

2.5.1 Time Resolution

In scintillator detectors, time resolution is the benchmark in precision. Time resolution describes how accurately a detector can determine when an event occurs. With two detectors and four PMTs, each acquisition produces four arrival times t_1, t_2 for bar A and t_3, t_4 for bar B.

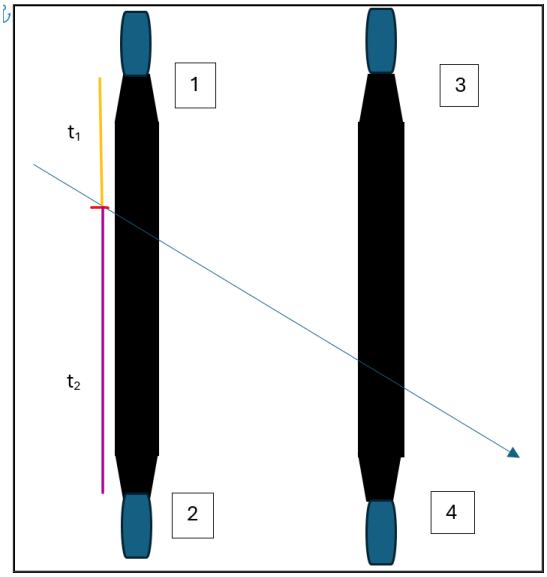

Figure 3: Schematic view of incident muon on both scintillator. t_1 and t_2 are the times it takes the photon to travel to both PMTs.

The arrival times can be written as:

$$t_1 = T_{0,A} + \frac{l/2 - y}{v_{\text{eff}}} \tag{7}$$

$$t_2 = T_{0,A} + \frac{l/2 + y}{v_{\text{eff}}} \tag{8}$$

where $T_{0,A}$ is a constant per bar for delays like cable length, y is hit position and l is length of the bar. Adding the two times cancels the position:

$$\frac{t_1 + t_2}{2} = T_{0,A} + \frac{l}{2 \cdot v_{\text{eff}}} \tag{9}$$

The arrival time of the bar is therefore independent of position. Because the right term in Equation 9 cancels out, the time between bars becomes:

$$\Delta t = (\frac{t_1 + t_2}{2}) - (\frac{t_3 + t_4}{2}) \tag{10}$$

From the 5000 measured values of Δt, the standard deviation of their distribution represents the detector's time resolution σ_t.

2.5.2 Effective light velocity in the scintillator

Photons produced in the scintillator do not propagate in a straight line to the PMTs. Instead, they undergo multiple reflections on the bar surfaces. Firstly, the speed of light in the scintillator material is $v_{\text{eff}} = c/n$, where n is the plastic's refractive index.
The time difference in a given bar is:

$$\Delta t_{\text{bar}} = t_1 - t_2 \tag{11}$$

The distribution of Δt_{bar} for 5000 acquisitions shows two peaks, corresponding to muons crossing near each end of the bar. By fitting these peaks with Gaussians, their mean positions are obtained. For a bar of length l the time difference between these peaks is approximately

$$\mu_2 - \mu_1 = \frac{2l}{v_{\text{eff}}} \tag{12}$$

The effective velocity is then equal to

$$v_{\text{eff}} = \frac{2l}{\mu_2 - \mu_1} \tag{13}$$

This value can then be compared to the expectation c/n.

2.5.3 Spatial Resolution

The spatial resolution of the detector describes how precisely the interaction point along the scintillator can be determined. The position along the scintillator can be described by:

$$y = \frac{v_{\text{eff}}}{2}(t_i - t_j) \tag{14}$$

Where i = [1,3] and j = [2,4].
The uncertainty and therefore the spatial resolution follow from the time resolution of a single bar.

$$\sigma_y = v_{\text{eff}} * \sigma_{t,bar} \tag{15}$$

2.5.4 Energy Determination

In a time-of-flight measurement, the energy of a charged particle can be derived from its measured flight time T between two scintillator detectors separated by distance L. The particle velocity is then:

$$v = \frac{L}{T} \tag{16}$$

From this the energy can be derived.

$$E = \frac{1}{2}mv^2 = \frac{1}{2}m\left(\frac{L}{T}\right)^2 \tag{17}$$

The uncertainty in the energy is related to the time resolution of the system.

$$\frac{\Delta E}{E} = 2\frac{\Delta T}{T} \tag{18}$$

[3] This equation shows that improving the time resolution or increasing the distance between detectors will result in a better energy resolution.

3 Experimental Methods

3.1 Experimental Setup

The experimental setup consists of five plastic scintillator detectors. Every measurement, two of these detectors are active. The downward cosmic muons should only be detected when the trajectory goes through both scintillators. The scintillators have the dimensions 50x10x10cm. Cosmic muons pass through the detectors without significant energy loss. This means that when the distance between detectors is increased, there is no need to remove the detectors in between. The XP2262 PMTs are connected to the high voltage supply CAEN SY 1527 Universal Multichannel Power Supply System. This voltage supply delivers a constant 1550 $\pm$ 1V to power the PMTs. To analyze the signal from the PMTs, the analog signal is digitized by the Agilent DC282 Digitizer.

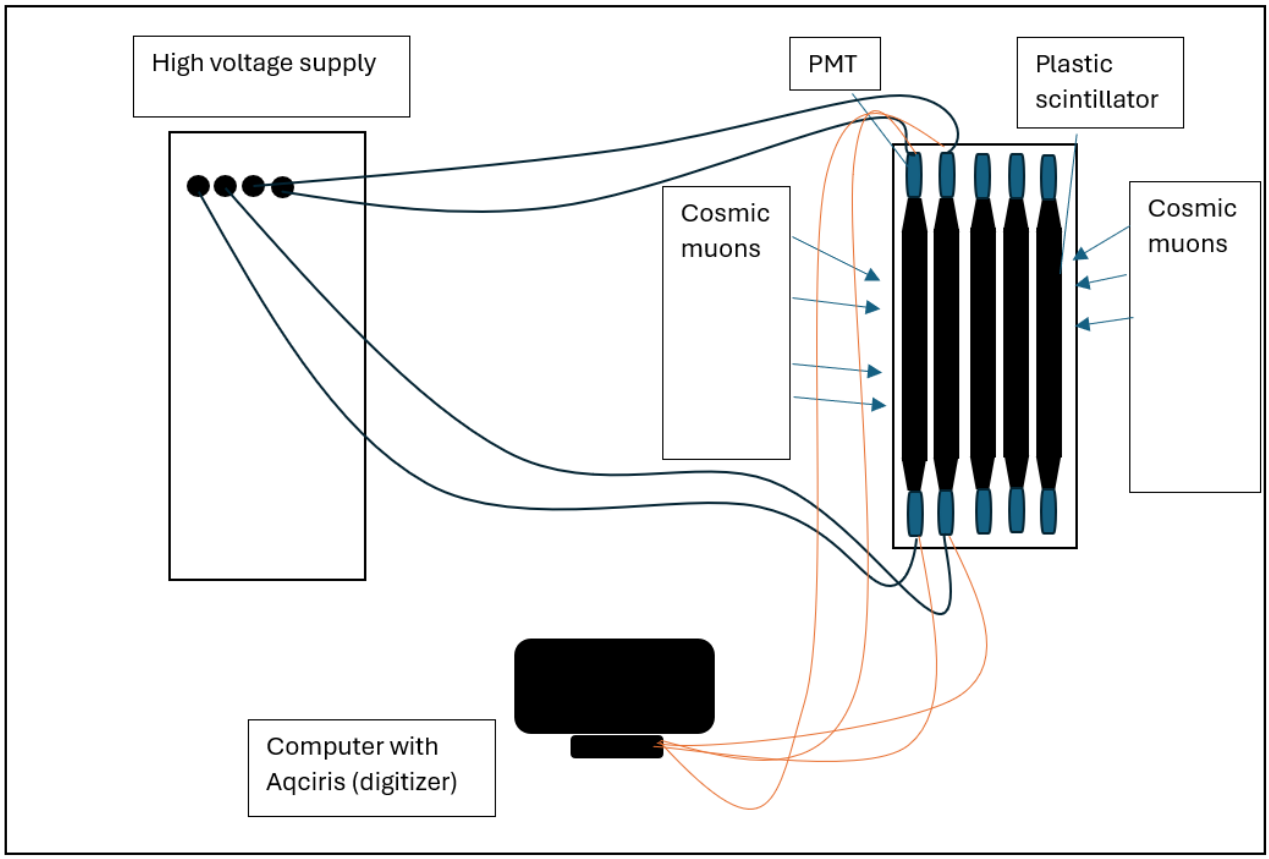

Figure 4: Schematic of Experimental Setup.

3.2 Software Configuration

The software configuration is important as there are many muons hitting the two scintillators; however, only the muons hitting both scintillators should result in an acquisition. In Acqiris software, the instrument settings are intended for this purpose. The Full Scale was set to 1V. The time window (x-axis) was set to 400 ns to see all pulses on the screen. The Trigger Delay was set to -150 ns to place the trigger at x = 0. The sampling rate was the maximum 2 GS/s; this allows the best digital representation of the analog pulse that is coming in. The Trigger Class was OR and the Trigger Source of all 4 channels should be *On* to ensure that only acquisitions where all 4 channels are triggered

are recorded. This is controversial as normally the AND-trigger would give us the required result. However, because of unknown complications inside the software, the OR-trigger gave the correct data. Furthermore, all 4 channels have the same Threshold of -11mV as the pulses are negative and background noise should be filtered.

3.3 Measurement Procedure

The detectors are all set in a case where one board has all cable inputs. The leftmost detector in Figure 4 is labeled 55; the next one to the right is 45, and so on up to 15. The 4 high voltage cables will be connected then to 55U, 55D, 45U, 45D, where 55U is the upper PMT and 55D is the lower PMT. The BNC cables should be connected to the board at inputs to 55U, 55D, 45U, 45D. 55U is connected to channel 1, 55D to channel 2, 45U to channel 3 and 45D to channel 4. If all channels are shown in the live window of the software, the acquisitions can be stored with the AutoStore function. Every measurement consists of 5000 acquisitions to get a precise time resolution. The same procedure is repeated for the other detectors.

4 Results

4.1 Overview of Data Processing

The digitizer records the data in .h5 format. To analyze this data, it is converted to .csv files. The converted data reveal negative pulses across all four channels for 5000 acquisitions. This data forms the basis for the analysis presented in the following sections.

Spacing (cm)	Measurement Duration
0	2 hours 20 minutes
10	14 hours 13 minutes
20	21 hours 10 minutes
30	8 days 21 hours 55 minutes

Table 1: Measurement duration required to complete 5000 acquisitions at each detector spacing.

4.2 Baseline Correction

Each PMT produces a waveform, however, the signal baselines are not identical across all channels. This makes it necessary to perform a baseline correction as precise data is necessary to investigate timing properties. The baseline is corrected by computing the average of the first 200 samples and subtracting this value from the entire pulse, thereby shifting the baseline to zero. After investigation of many acquisitions, the earliest scintillator pulses start after 200 counts. Using 200 samples improves the statistical precision of the baseline estimate compared to a shorter window.

Figure 5b presents the original pulses from all PMTs, where the baseline of Channel 3 is slightly lower than that of the others. This offset is corrected in the adjusted pulses shown in Figure 5b. The deviation of the adjusted signal is relatively small, therefore Figure 6 shows it in more detail.

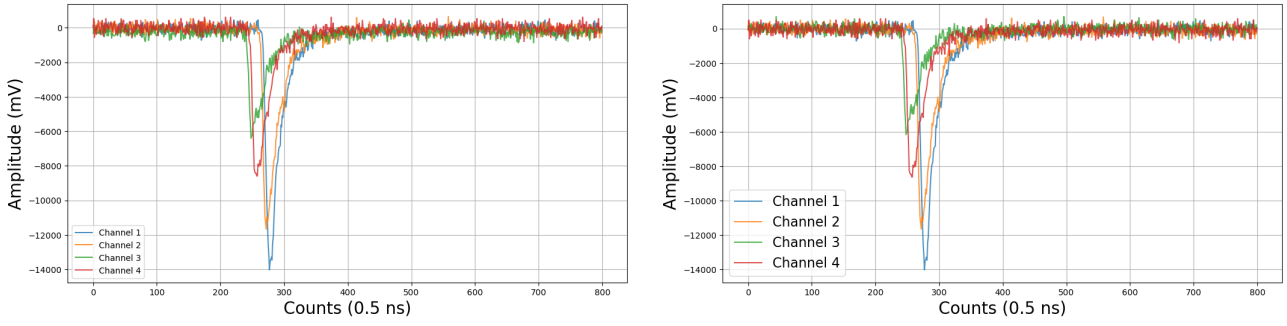

(a) Original pulses

(b) Adjusted pulses

Figure 5: Baseline correction for all channels for pulse 1 of measurement with 20 cm separation.

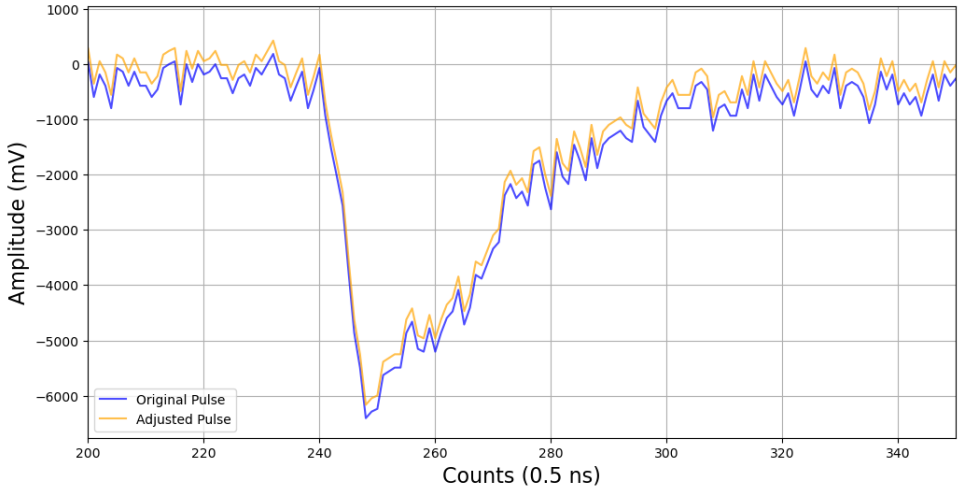

Figure 6: Closer look at baseline correction in channel 3.

4.3 Gain Matching

Figure 7 presents the pulse-integral spectra of the two PMTs on one bar. The offset between their peaks reflects a gain difference, which is corrected by forming the geometric mean shown in Figure 8.

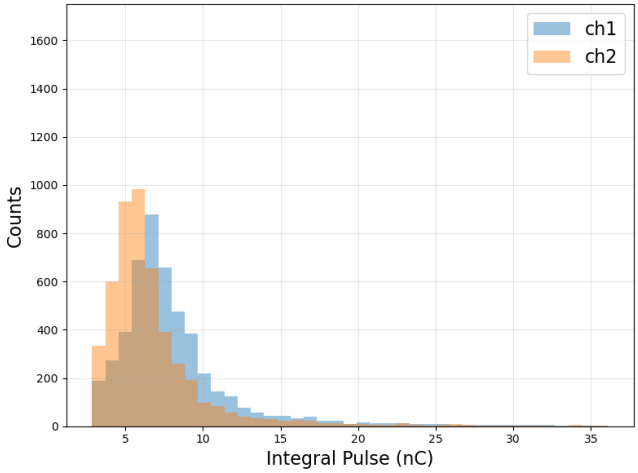

Figure 7: Integrated pulse area for both PMTs of detector A.

In Figure 8 channels 1 and 2 correspond to bar A, and channels 3 and 4 correspond to bar B. The resulting spectrum shows that the peaks of both detectors are not aligned. As both bars are exposed to the same particle flux, the peaks should be in the same position. The observed offset is therefore attributed to a difference in gain between the detectors.

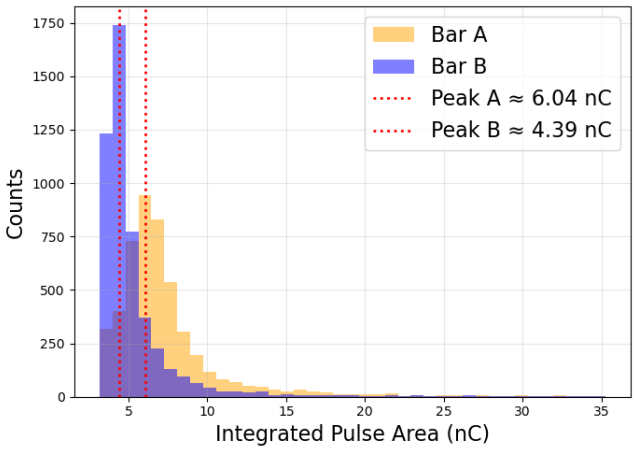

Figure 8: Geometric mean of channels' integrated pulse area for measurement with 20 cm separation.

A gain matching procedure was applied to correct for this mismatch.

$$\text{Gain correction factor} = \frac{\text{Peak bar A}}{\text{Peak bar B}} \tag{19}$$

To validate the matching, a heatmap of the pulse integrals from bar A and B was constructed. The distribution aligns along the diagonal, confirming that the offset was successfully removed.

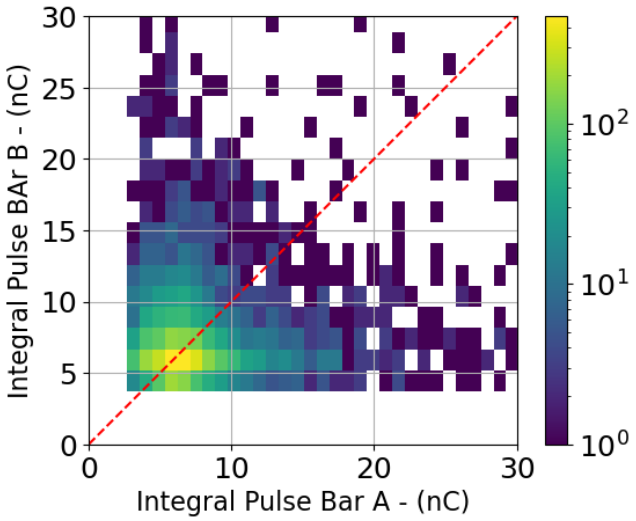

Figure 9: Heatmap of integrated pulse area per bar to validate gain equalization.

4.4 CFD Optimization

To determine the optimal CFD parameters, the time resolution per bar is evaluated for each combination of delay and fraction. For every pair of parameters, the CFD algorithm is applied to all 5000 waveforms, giving one zero-point per waveform and per bar. From these zero-points, the bar-bar time differences Δt are calculated and filled into a histogram. From this the time resolution per bar is calculated and stored in a table for all delay-fraction combinations. Figure 10 shows this table as a heatmap, the minimum indicated the optimal parameters. The optimal configuration was found at a delay of 11 counts and a fraction of 0.35.

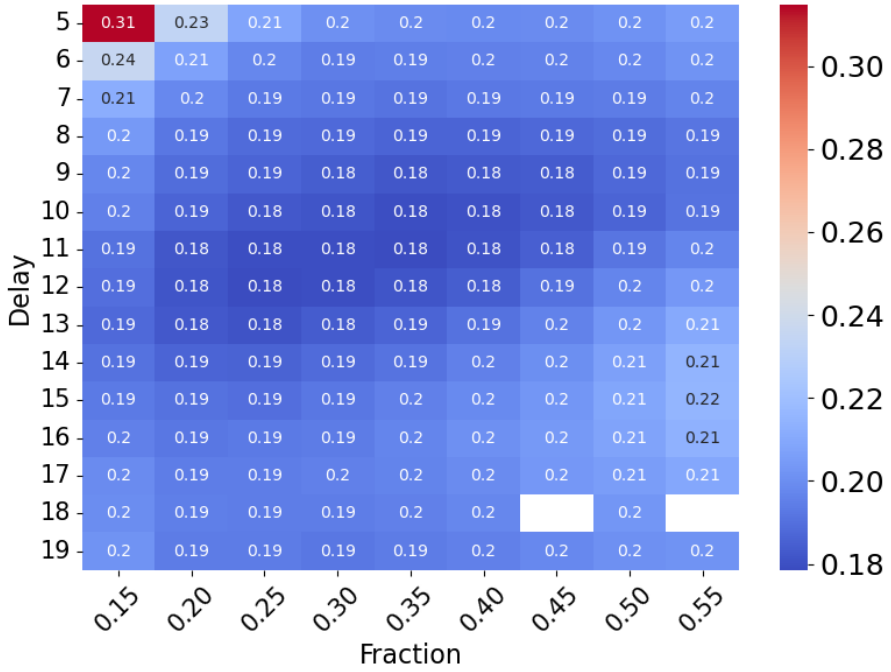

Figure 10: σ_t per-bar for different CFD parameters. White boxes are out of bounds.

4.5 Determination of Effective Velocity

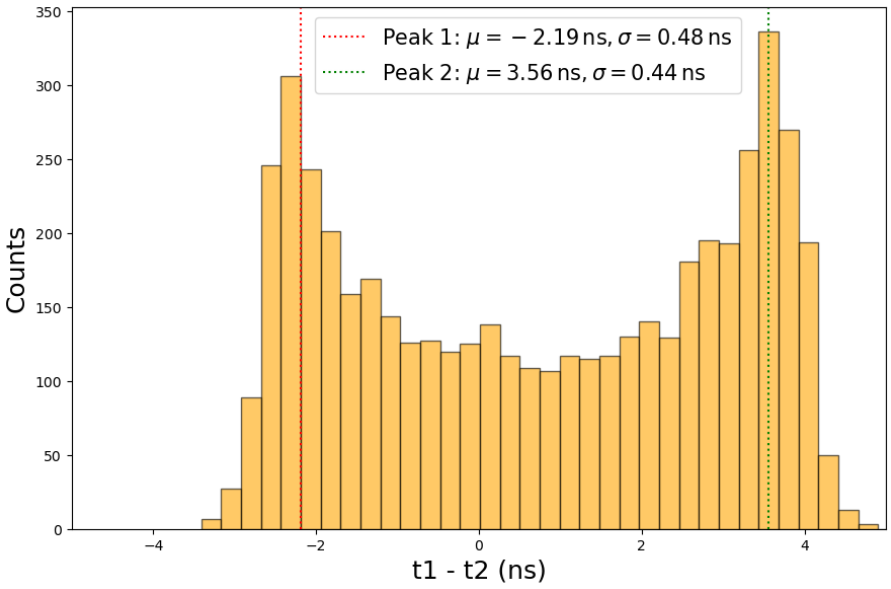

Figure 11: Time difference in a single bar.

From Equation 13, the effective velocity of photons inside the scintillator bar is

$$v_{\text{eff}} = \frac{100 \text{ cm}}{3.56 - (-2.19) \text{ ns}} \approx 17.4 \pm 2 \text{ cm/ns}$$

The uncertainty on v_{eff} follows from the fit uncertainties on μ_1 and μ_2 (Appendix B).

4.6 Determination of Resolutions

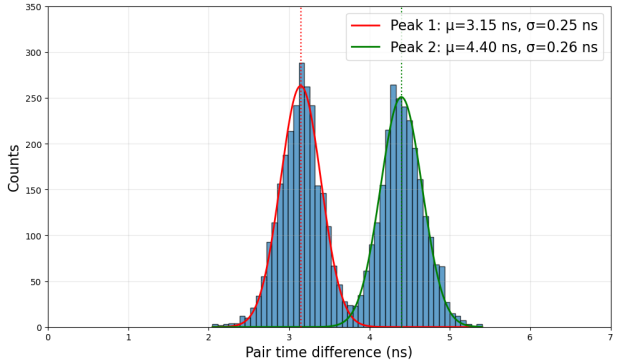

(a) No separation

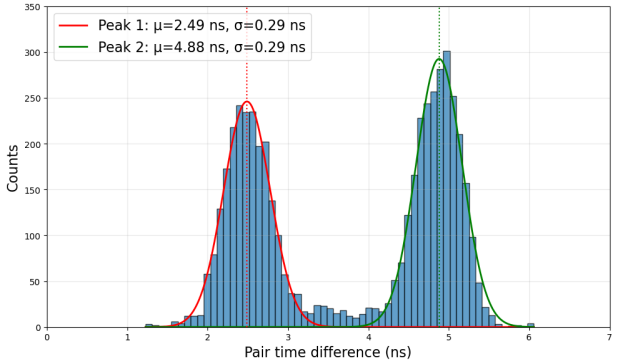

(b) 10 cm separation

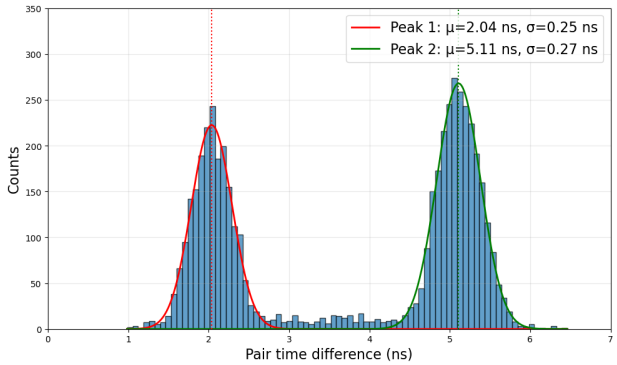

(c) 20 cm separation

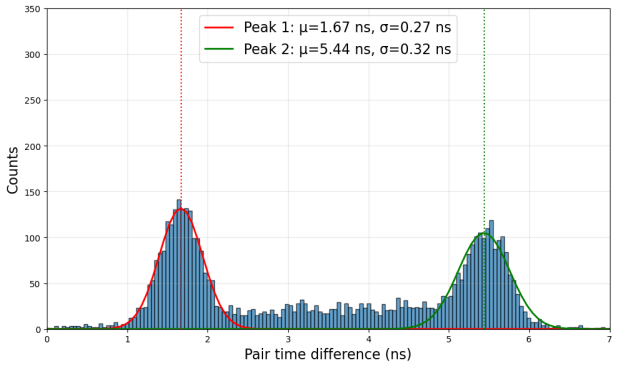

(d) 30 cm separation

Figure 12: Histograms of time differences with double-Gaussian fits for time resolution estimation.

The pair time difference distributions are bimodal for all separations. This is due to the double detector geometry. The two peaks correspond to the traversal ordering (detector A first and detector B first). To estimate the time resolution σ_t every peak is fitted with a Gaussian. The per-bar time resolution is the equal to

$$\sigma_{t,bar} = \frac{\sigma_{t,pair}}{\sqrt{2}} \tag{20}$$

As $\sigma^2_{t,pair} = 2\sigma^2_{t,bar}$. Where $\sigma_{t,pair}$ is the average of the two peaks' width.
From Equation 15, the uncertainty in position can be determined per bar.

Spacing (cm)	σ_t left (ns)	σ_t right (ns)	σ_t per bar (ns)	$\sigma_y \pm 0.4$ (cm)
0	0.25	0.26	0.181	3.2
10	0.29	0.29	0.204	3.6
20	0.24	0.27	0.179	3.1
30	0.27	0.32	0.208	3.6

Table 2: Timing and spatial resolution versus detector separation

5 Discussion

5.1 Accuracy of Experiment

5.1.1 Gain Matching

Because the geometric mean provides a position-independent estimate of the deposited energy, the expectation is that the spectrum of E_{bar} is narrower than the spectra of E_1 and E_2. However in Figure 7 and 8, this sharpening is minimal. The spectra of the two PMTs in one bar show similar widths but different peak positions because of the difference in gain. After applying the geometric mean, the width of the bar spectrum is not much smaller. This indicates that the main contributions to broadening are not position-dependent. Overall the geometric mean is still a meaningful energy estimator and the successful gain matching gives a comparable output scales to both bars.

Gain matching has been implemented via software. It was also attempted to correct the gains of the PMTs by increasing the supply voltages. The peaks in the histogram for the integral pulse area for single channels were taken into account. The supply voltages were increased for the PMTs for which the peaks were at a lower integral. This approach did not result in closer peaks due to differences in the detectors. Therefore, a software-based solution was applied.

5.1.2 CFD

The optimal parameters for CFD can vary for different separations. To ensure consistent results, it was decided to use the same parameters for all separations. This allows the zero points of the pulses to be analyzed most effectively and therefore the resolutions for each separation.

The results of our CFD optimization are consistent with theoretical expectations. The delay should be chosen on the order of the pulse rise time. In our experiment the mean rise time was 14 counts. In our heatmap, it is shown that the delay around this value results in the lowest time resolution. The minimum delay-fraction in Figure 10 is not a single sharp point but a broad plateau. Several combinations give time resolutions that differ less than a few picoseconds. This means that the global minimum is well defined, while the timing performance is not super sensitive to small changes of the CFD parameters.

5.1.3 Effective Velocity

The effective velocity extracted from the measurements was established at $v_{\text{eff, meas}} = 17.4 \pm 2$ cm/ns, while the theoretical value is $v_{\text{eff, theory}} = 18.9$ cm/ns. The theoretical value assumes a straight line in the scintillator to the PMTs. However, in reality, scintillation light travels via a combination of direct paths and many reflections on the plastic surfaces. Therefore, the length of these paths is longer than a straight line, therefore taking longer to reach the PMTs, lowering the effective velocity. The lower value in measurements is therefore consistent with realistic photon transport in a plastic bar.

When fitting the Gaussians in the histogram, only a limited time window was used. The full histogram contains a broad distribution between the two peaks because many muons pass through the middle of the scintillator bar. Including this central region prevents a Gaussian fit from converging as the peak is not isolated enough. To ensure a meaningful fit, an interval of approximately 1.5 ns around each peak

was selected. In this interval, the peak is sufficiently sharp to be described by a Gaussian, allowing us to extract the mean and standard deviation.

5.2 Importance of Timing Accuracy

In time-of-flight measurements, precise timing is crucial as the particle's energy is derived from its flight time. Equation 18 shows that the relative energy resolution is proportional to the timing resolution. In other words, a long flight path and a small timing uncertainty results in a small energy uncertainty.

Timing precision also drives the spatial properties when using plastic scintillator detector setups. In our geometry, the hit position is determined from the difference in times between PMTs at both ends. The uncertainty in position scales like Equation 15. Thus high timing uncertainty results in high spatial uncertainty.

As the detector spacing increases, the coincidence rate is traded for angular selection. At small separations, coincidences are frequent and 5000 acquisitions can be collected in a few hours; however, the geometry accepts more vertical trajectories. Increasing the separation filters out these vertical trajectories, giving a better-defined interaction position and a geometry that is closer to n_TOF conditions. However, this results in a strong drop in coincidence rate: at the largest separation, 5000 acquisitions took almost 9 days to record. Therefore, the optimum balance was found at 20 cm separation. This separation selects mostly perpendicular trajectories, while still allowing 5000 acquisitions to be recorded within 22 hours. Also, this separation gave us the best resolutions.

Additionally, the data show that bar A is triggered first more frequently than bar B. As muons come falling from space, it should be an equal distribution. The asymmetry can be explained by the placement of the plastic scintillator detector's case. Bar B was placed closer to a concrete wall, while bar A was closer to a window. Lower-energy muons are more easily absorbed by the wall and will therefore not be detected. This results in a slightly higher flux and earlier triggers on bar A.

5.3 Application at n_TOF

This experiment used cosmic muons instead of recoil protons, which are used at n_TOF. The results still provide valuable insight into detector behavior for time-of-flight applications. Cosmic-ray muons are suited quite well for this purpose. They can penetrate easily through both scintillator bars to produce clear signals. Their energy is typically a few GeV, meaning they deposit nearly the same amount of energy in the scintillator each time they pass through. This stable light production allows for precise study without the need for a particle beam. Muons travel at relativistic speeds, which makes any variation in time difference a result of detector properties. For these reasons, muons provide a reliable substitute for recoil protons for the investigation of plastic scintillator detectors.

At n_TOF, the plastic scintillator detectors studied in this work would be used in the proton recoil telescope, where recoil protons travel about 5 m between the start and stop detectors. For protons in the 20 MeV - 1 GeV range this corresponds to flight times of about 80 - 20 ns. With a measured per-bar time resolution of 0.18 ns, the coincidence time resolution of a start-stop pair is 0.25 ns. Inserting this in Equation 18, gives a fractional energy resolution between $6 \cdot 10^{-3}$ and $3 \cdot 10^{-2}$. The timing performance of plastic scintillator detectors therefore allows a percent-level energy resolution

for recoil protons. Therefore, it can be stated that these detectors are suitable for the n_TOF proton recoil telescope.

6 Conclusion

In this work, the performance of plastic scintillator detectors was investigated for application at CERN's n_TOF facility. Using cosmic muons, multiple detector separations were used to study the time and spatial resolution. 5000 acquisitions per separation were analyzed using baseline correction, gain matching and constant fraction discrimination to determine the optimal conditions to deduce detector properties.

The results of this experiment are promising. The detectors showed stable operation across all measurements. The time resolution achieved for all separations demonstrates the excellent performance of these detectors. Larger separations select more perpendicular tracks; however, the coincidence rate is drastically reduced. A separation of 20 cm was found to provide the best balance, resulting in a time resolution per-bar of 0.18 ns and a spatial resolution of approximately 3.1 ± 0.4 cm.

When applying these results to n_TOF, the 5 m flight path of the recoil protons in the proton recoil telescope means that the same timing precision corresponds to a fractional energy uncertainty at the level of about one percent or below. This confirms that the intrinsic timing performance of plastic scintillator detectors is excellent for time-of-flight measurements at n_TOF.

Future research could build on this work by testing the same detector setup with a neutron beam at the n_TOF facility to confirm the timing performance. It could compare the response of cosmic muons and recoil protons and identify any effects from neutron scattering.

Bibliography

[1] C. Guerrero, A. Tsinganis, E. Berthoumieux, M. Barbagallo, F. Belloni, F. Gunsing, C. Weiß, E. Chiaveri, M. Calviani, V. Vlachoudis, S. Altstadt, S. Andriamonje, J. Andrzejewski, L. Audouin, V. Bécares, F. Bečvář, J. Billowes, V. Boccone, D. Bosnar, and . other authors ...], "Performance of the neutron time-of-flight facility n_tof at cern," *European Physical Journal A*, vol. 49, p. 27, 2013.

[2] A. Manna, S. Amaducci, M. Barbagallo, N. Colonna, L. Cosentino, P. Finocchiaro, S. L. Meo, C. Massimi, M. Mastromarco, P. M. Milazzo, F. Mingrone, L. Tassan-Got, G. Vannini, and A. Ventura, "A proton recoil telescope for the characterisation of the neutron beam at n_tof," *Il Nuovo Cimento C*, vol. 42, no. 142, 2019. On behalf of the n_TOF Collaboration.

[3] K. Koizumi *et al.*, "Demonstration of shape analysis of neutron resonance-spectrum measurement," *Scientific Reports*, vol. 14, no. 1, p. 14875, 2024.

[4] S. Tavernier, *Experimental Techniques in Nuclear and Particle Physics*. 2010.

[5] Hamamatsu Photonics K.K., *Photomultiplier Tubes: Basics and Applications*. Hamamatsu City, Japan: Hamamatsu Photonics K.K., 3rd ed., 2007.

[6] E. C. Samaranayake, T. S. Senanayake, W. S. Hewage, G. D. Raju, L. M. Wickramarathna, S. M. Ragama, P. A. C. Wickramarachchi, J. D. D. R. Prematilake, P. D. Pathirathna, T. M. A. Tennakoon, T. R. D. Chaturanga, M. Liyanage, and S. M. Dissanayake, "Measurement of time resolution in plastic scintillators using constant fraction discrimination," *Nuclear Instruments and Methods in Physics Research Section A*, vol. 1027, p. 166050, 2022.

[7] A. Blondel, A. Bravar, A. Damyanova, A. Ereditato, M. Hildebrandt, I. Kreslo, T. Seraganian, P. Scampoli, M. Studer, and M. Weber, "Timing characteristics of 3-meter long scintillator bars read out with large area sipms using waveform digitizers," *Nuclear Instruments and Methods in Physics Research Section A*, vol. 877, pp. 9–15, 2018.

[8] T. K. Gaisser, R. Engel, and E. Resconi, *Cosmic Rays and Particle Physics*. Cambridge University Press, 2nd ed., 2016.

[9] R. L. Workman and O. P. D. Group), "Review of particle physics," *Progress of Theoretical and Experimental Physics*, vol. 2024, no. 8, p. 083C01, 2024. Sections on Cosmic Rays and Muon properties.

[10] E. V. Bugaev, A. Misaki, V. A. Naumov, T. S. Sinegovskaya, S. I. Sinegovsky, and N. Takahashi, "Atmospheric muon flux at sea level, underground, and underwater," *Physical Review D*, vol. 58, p. 054001, 1998.

[11] J. Zhao, B. Sun, I. Tanihata, S. Terashima, L. Zhu, A. Enomoto, D. Nagae, T. Nishimura, S. Omika, A. Ozawa, Y. Takeuchi, and T. Yamaguchi, "Reaching time resolution of less than 10 ps with plastic scintillation detectors," *Nuclear Instruments and Methods in Physics Research Section A: Accelerators, Spectrometers, Detectors and Associated Equipment*, vol. 823, pp. 41–46, 2016.

[12] S. Brünner, L. Gruber, J. Márton, K. Suzuki, and A. Hirtl, "New approaches for improvement of tof-pet," *Nuclear Instruments and Methods in Physics Research Section A: Accelerators, Spectrometers, Detectors and Associated Equipment*, vol. 732, pp. 560–563, 2013.

[13] G. F. Knoll, *Radiation Detection and Measurement*. Wiley, 4th ed., 2010.

[14] F. Loddo and C. Tamma, "Constant fraction discriminator," in *VFAT3 Status Meeting*, 2013.

Appendices

A Analysis Code

For the complete source code, see the repository in `github`.

B Error Propagation

B.1 Effective Velocity

The effective velocity is given by

$$v_{\text{eff}} = \frac{2l}{\Delta\mu}, \qquad \Delta\mu = \mu_2 - \mu_1.$$

The uncertainty on v_{eff} follows from the uncertainties in the fitted peak means μ_1 and μ_2. Using standard error propagation,

$$\sigma^2_{v_{\text{eff}}} = \left(\frac{\partial v_{\text{eff}}}{\partial \mu_1}\sigma_{\mu_1}\right)^2 + \left(\frac{\partial v_{\text{eff}}}{\partial \mu_2}\sigma_{\mu_2}\right)^2.$$

With

$$\frac{\partial v_{\text{eff}}}{\partial \mu_1} = \frac{2l}{(\Delta\mu)^2}, \qquad \frac{\partial v_{\text{eff}}}{\partial \mu_2} = -\frac{2l}{(\Delta\mu)^2},$$

this gives

$$\sigma_{v_{\text{eff}}} = \frac{2l}{(\Delta\mu)^2}\sqrt{\sigma^2_{\mu_1} + \sigma^2_{\mu_2}}.$$

B.2 Spatial Resolution

The spatial resolution per bar is given by

$$\sigma_y = v_{\text{eff}}\,\sigma_{t,\text{bar}}.$$

Since only the uncertainty in v_{eff} is considered, standard error propagation gives

$$\sigma^2_{\sigma_y} = \left(\frac{\partial \sigma_y}{\partial v_{\text{eff}}}\sigma_{v_{\text{eff}}}\right)^2.$$

Because

$$\frac{\partial \sigma_y}{\partial v_{\text{eff}}} = \sigma_{t,\text{bar}},$$

the uncertainty becomes

$$\sigma_{\sigma_y} = \sigma_{t,\text{bar}}\,\sigma_{v_{\text{eff}}}.$$